

SCALING RELATIONS AND X-RAY PROPERTIES OF MODERATE-LUMINOSITY GALAXY CLUSTERS FROM $0.3 < z < 0.6$ WITH *XMM-NEWTON*¹

THOMAS CONNOR^{2,3}, MEGAN DONAHUE², MING SUN⁴, HENK HOEKSTRA⁵, ANDISHEH MAHDAVI⁶, CHRISTOPHER J. CONSELICE⁷, AND BRIAN MCNAMARA^{8,9,10}

Accepted for publication in The Astrophysical Journal

ABSTRACT

We present new X-ray temperatures and improved X-ray luminosity estimates for 15 new and archival *XMM-Newton* observations of galaxy clusters at intermediate redshift with mass and luminosities near the galaxy group/cluster division ($M_{2500} < 2.4 \times 10^{14} h_{70}^{-1} M_{\odot}$, $L < 2 \times 10^{44} \text{ erg s}^{-1}$, $0.3 < z < 0.6$). These clusters have weak-lensing mass measurements based on *Hubble Space Telescope* observations of clusters representative of an X-ray selected sample (the *ROSAT* 160SD survey). The angular resolution of *XMM-Newton* allows us to disentangle the emission of these galaxy clusters from nearby point sources, which significantly contaminated previous X-ray luminosity estimates for six of the fifteen clusters. We extend cluster scaling relations between X-ray luminosity, temperature, and weak-lensing mass for low-mass, X-ray-selected clusters out to redshift ~ 0.45 . These relations are important for cosmology and the astrophysics of feedback in galaxy groups and clusters. Our joint analysis with a sample of 50 clusters in a similar redshift range but with larger masses ($M_{500} < 21.9 \times 10^{14} M_{\odot}$, $0.15 \leq z \leq 0.55$) from the Canadian Cluster Comparison Project finds that within r_{2500} , $M \propto L^{0.44 \pm 0.05}$, $T \propto L^{0.23 \pm 0.02}$, and $M \propto T^{1.9 \pm 0.2}$. The estimated intrinsic scatter in the M-L relation for the combined sample is reduced to $\sigma_{\log(M|L)} = 0.10$, from $\sigma_{\log(M|L)} = 0.26$ with the original *ROSAT* measurements. We also find an intrinsic scatter for the T-L relation, $\sigma_{\log(T|L)} = 0.07 \pm 0.01$.

Subject headings: galaxies: clusters: general — X-rays: galaxies: clusters

1. INTRODUCTION

Simulations of cosmological structure formation show clusters and filaments of dark matter growing from a set of random initial perturbations into a cosmic web (e.g. Springel et al. 2005; Boylan-Kolchin et al. 2009; Klypin et al. 2011). The statistical properties of this cosmic web are extremely sensitive to the values of certain cosmological parameters, particularly Ω_M and σ_8 , the amplitude of the initial perturbation spectrum (e.g. Eke et al. 1996; Bahcall & Fan 1998; Holder et al. 2001; Allen et al. 2011).

This cosmic web of dark matter is easiest to investigate by studying its most massive systems, which are clusters of galaxies. About 85% of a cluster’s mass is composed of dark matter, while nearly all of the rest is

intergalactic hot gas, with a trace amount contributed by stars (Rosati et al. 2002; Voit 2005; LaRoque et al. 2006). The hot gas is confined by the cluster’s gravitational potential and radiates X-rays, providing powerful diagnostics for properties of the host cluster, including its mass, baryonic content, and dynamic status.

Accurate measurements of galaxy cluster masses are useful for more than just describing individual systems; galaxy cluster masses are needed to verify models of large-scale structure formation (Jenkins et al. 2001; Grossi et al. 2007; Vikhlinin et al. 2009) and to constrain cosmological parameters (Tinker et al. 2008; Rozo et al. 2010; Mantz et al. 2010; Bhattacharya et al. 2011). One way to accurately measure the projected mass of a cluster is through measurements of gravitational lensing (Hoekstra et al. 2013). However, performing such measurements is prohibitively expensive for large samples of clusters and difficult for low redshift clusters. To this end, scaling relations have been empirically calibrated to connect observed properties to masses. Examples of this include $L_X - M_X$, $M_X - T_X$, and $M_X - Y_X$ relations.

Early work by Kaiser (1986) showed that these relations can be cast analytically for the case where cold gas falls into preexisting dark matter structures. Those early relations predicted clusters that were overluminous for a given temperature compared to observations. So Kaiser (1991) and Evrard & Henry (1991) showed that preheating could increase the entropy of intergalactic gas. Such a “preheating” model elevates the entropy of the gas, preventing the gas from getting too dense. These predicted $L_X - M_X$ and $T_X - M_X$ relations were roughly consistent with observations. This expectation that clusters would follow such laws over a

¹ Based on observations obtained with *XMM-Newton*, an ESA science mission with instruments and contributions directly funded by ESA Member States and NASA

² Department of Physics and Astronomy, Michigan State University, East Lansing, MI 48823, USA

³ connort1@msu.edu

⁴ Department of Physics, University of Alabama in Huntsville, Huntsville, AL 35899, USA

⁵ Leiden Observatory, Leiden University, PO Box 9513, 2300 RA, Leiden, the Netherlands

⁶ Department of Physics and Astronomy, San Francisco State University, San Francisco, CA 94131, USA

⁷ University of Nottingham, School of Physics and Astronomy, Nottingham NG7 2RD, UK

⁸ Department of Physics and Astronomy, University of Waterloo, 200 University Avenue West, Waterloo, Ontario N2L 5M3, Canada

⁹ Perimeter Institute for Theoretical Physics, 31 Caroline Street, Waterloo, Ontario N2L 2Y5, Canada

¹⁰ Harvard-Smithsonian Center for Astrophysics, Cambridge, MA 02138, USA

large range of M_X , with standard evolutionary factors, is known as self-similarity (Navarro et al. 1997; Bower 1997; Bryan & Norman 1998). The scale-free nature of this behavior arises because the gravitational potential dominates over other energy sources, and gravity is scale-free.

Previous work has shown possible deviations from self-similarity at masses approaching those of galaxy groups (e.g. Ponman et al. 1996; Xue & Wu 2000; Eckmiller et al. 2011; Stott et al. 2012), possibly due to the increasing fractional contribution of local feedback processes to the cluster energy budget compared to the gravitational potential. The exact magnitude and behavior of this deviation is not yet defined, but it has been qualitatively reproduced in numerical work (Puchwein et al. 2008; Fabjan et al. 2010).

A full understanding of the deviation from self-similarity can only come through a thorough exploration of the cluster parameter space – across cluster mass ranges and redshifts. One under-sampled regime is at moderate redshift and low mass. Clusters with these properties offer us the ability to answer the questions of how scaling relations change from high redshift to low redshift and whether there is any evolution in the low-mass behavior of these relations.

Recent work by Hoekstra et al. (2011) provided weak lensing mass measurements from the *Hubble Space Telescope* (HST) of 25 galaxy clusters occupying this redshift regime. That work lacked high-quality X-ray observations for most of the objects, however. We use observations with the *XMM-Newton* satellite to study the X-ray characteristics of this sample and to constrain X-ray property and mass scaling relations for this redshift and mass regime.

The structure of this paper is as follows. In Section 2, we describe the properties of our sample, while our analysis techniques are described in Section 3. The results of our analysis are presented in Section 4. In particular, we discuss our fits of three scaling relations involving X-ray luminosity, temperature, and weak lensing mass. Finally, we compare our results to other published works in Section 5 and Appendix B. Throughout this paper, we assume a flat Λ CDM cosmology with $\Omega_M = 0.3$, and $H_0 = 70 \text{ km s}^{-1} \text{ Mpc}^{-1}$.

2. DATA AND ANALYSIS

Our sample is based on 25 galaxy clusters first detected in the *ROSAT* 160 Square Degree Survey. Vikhlinin et al. (1998) describe the initial survey, and a reanalysis with spectroscopic redshifts comes from Mullis et al. (2003). These 25 clusters were further studied with an HST snapshot program (PI: Donahue) of one orbit per cluster with the F814W filter. Due to the nature of the snapshot program, the clusters were randomly selected from a master list of 72 clusters. Hoekstra et al. (2011) used those images to estimate weak-lensing masses for these clusters. The focus of this work is to improve and augment the X-ray measurements of these clusters with observations with *XMM-Newton*. Along with new observations, we used archival data to supplement the cluster sample with new uniform measurements of X-ray properties.

We searched the archive of *XMM-Newton* observations with the XMM-Newton Science Archive (XSA)

v7.2 within a 15' radius of the cluster positions given in Hoekstra et al. (2011). As of June 28, 2013, we found 27 observations that included the cluster. We excluded 9 because they were too short and excluded 4 that were unusable due to excessive particle contamination from flares, leaving 14 observations of 11 clusters. We supplemented these with five new observations of four clusters. All observations were taken with the European Photon Imaging Camera (EPIC), which consists of two MOS cameras (Turner et al. 2001) and the pn camera (Strüder et al. 2001). Cluster properties drawn from earlier works are provided in Table 1. Hydrogen column density, N_H , is taken from the compilation by Kalberla et al. (2005). The datasets used in this work are listed in Table 2.

Our new observations are presented in Figure 1. Our data are shown as smoothed X-ray contours from combined EPIC images overlaid on HST images of the cluster using the Advanced Camera for Surveys / Wide Field Channel F814W filter. Combined X-ray products were created using the XMM-Newton Science Analysis System (SAS) `images` script binning to $2''$ and smoothing with a Gaussian FWHM of $15''$ in the energy range of 0.4 - 8.0 keV. Contours are levels of $10^{-6} \text{ counts s}^{-1} \text{ arcsec}^{-2}$, with the lowest displayed contour corresponding to $10^{-6} \text{ count s}^{-1} \text{ arcsec}^{-2}$ for RXJ0826.1+2625 and RXJ2059.9-4245 and $2 \times 10^{-6} \text{ count s}^{-1} \text{ arcsec}^{-2}$ for RXJ1642.6+3935 and RXJ2139.9-4305.

Observations were reduced using the XMM-Newton SAS version 12.0.1.¹¹ Bad time intervals were defined based on the count rate of high energy events ($>10 \text{ keV}$) in 100-second bins; time periods where those exceeded $0.35 \text{ count s}^{-1}$ (MOS) or $0.40 \text{ count s}^{-1}$ (pn) were excluded. One exception to this was the observation of RXJ1354.2-0221, 0112250101, which had an abnormally high high-energy background. To avoid overfiltering the data, we increased the count rate limits to 0.5 count s^{-1} (MOS) and $0.65 \text{ counts s}^{-1}$ (pn) for this observation only. For all observations the filtering levels were scrutinized to ensure that periods of significant flaring were entirely removed. When necessary, we made the high-energy count rate thresholds more stringent.

Point sources were detected using the individual tasks that make up `edetect_chain`. This task uses `eboxdetect` to perform a sliding box detection of sources with a local background, then has `esplinemap` generate a source-corrected global background, which a second run of `eboxdetect` uses to find sources again. Sources were selected from these detections by hand after a visual inspection. Table 3 lists the coordinates and radii of a sample of the sources; a full table is provided in the online edition. All identified sources were excluded from the spectral extraction regions.

We then extracted spectra from the observations in three different apertures using standard options ("`#XMMEA_EM`" for MOS data and "`#XMMEA_EP`" for pn). For all cameras we selected single and double events, filtering with "`PATTERN <12`" for MOS and "`PATTERN <4`" for pn. Our first aperture was $300 h_{70}^{-1} \text{ kpc}$, which was chosen to compare our measured fluxes against those of Vikhlinin et al. (1998). Our second aperture was a circle with radius equal to the value of r_{2500} given in Table 2 of Hoekstra et al. (2011). r_{2500} is the radius inside

¹¹ <http://xmm.esac.esa.int/sas/>

TABLE 1
SAMPLE PROPERTIES

Cluster Name	α_{2000}^a	δ_{2000}^a	α_{2000}^b	δ_{2000}^b	z^c	N_H^d 10^{20} cm^{-2}	r_{2500}^a $h_{70}^{-1} \text{ Mpc}$
RXJ0056.9–2740	00 ^h 56 ^m 56.98 ^s	–27°40 ^m 29.9 ^s	00 ^h 56 ^m 57.9 ^s	–27°40 ^m 29.3 ^s	0.563	1.79	0.270
RXJ0110.3+1938	01 ^h 10 ^m 18.22 ^s	+19°38 ^m 19.4 ^s	01 ^h 10 ^m 18.2 ^s	+19°38 ^m 18.7 ^s	0.317	3.82	0.293
RXJ0522.2–3625	05 ^h 22 ^m 15.48 ^s	–36°24 ^m 56.1 ^s	05 ^h 22 ^m 15.4 ^s	–36°24 ^m 55.7 ^s	0.472	3.63	0.313
RXJ0826.1+2625	08 ^h 26 ^m 08.03 ^s	+26°25 ^m 16.7 ^s	0.351	3.39	0.157
RXJ0847.1+3449	08 ^h 47 ^m 11.79 ^s	+34°48 ^m 51.8 ^s	08 ^h 47 ^m 11.7 ^s	+34°48 ^m 51.9 ^s	0.560	2.92	0.452
RXJ0957.8+6534	09 ^h 57 ^m 51.22 ^s	+65°34 ^m 25.1 ^s	09 ^h 57 ^m 51.1 ^s	+65°34 ^m 26.1 ^s	0.530	5.32	0.257
RXJ1117.4+0743	11 ^h 17 ^m 26.04 ^s	+07°43 ^m 38.3 ^s	11 ^h 17 ^m 26.1 ^s	+07°43 ^m 41.0 ^s	0.477	3.59	0.280
RXJ1354.2–0221	13 ^h 54 ^m 17.19 ^s	–02°21 ^m 59.0 ^s	13 ^h 54 ^m 17.2 ^s	–02°21 ^m 59.4 ^s	0.546	3.22	0.428
RXJ1642.6+3935	16 ^h 42 ^m 38.35 ^s	+39°36 ^m 10.4 ^s	16 ^h 42 ^m 38.4 ^s	+39°36 ^m 07.9 ^s	0.355	1.20	0.239
RXJ2059.9–4245	20 ^h 59 ^m 54.92 ^s	–42°45 ^m 32.1 ^s	20 ^h 59 ^m 54.9 ^s	–42°45 ^m 34.8 ^s	0.323	3.13	0.280
RXJ2108.8–0516	21 ^h 08 ^m 51.17 ^s	–05°16 ^m 58.4 ^s	21 ^h 08 ^m 51.2 ^s	–05°16 ^m 57.6 ^s	0.319	6.30	0.210
RXJ2139.9–4305	21 ^h 39 ^m 58.22 ^s	–43°05 ^m 13.9 ^s	21 ^h 39 ^m 58.3 ^s	–43°05 ^m 14.2 ^s	0.376	1.63	0.292
RXJ2146.0+0423	21 ^h 46 ^m 05.52 ^s	+04°23 ^m 14.3 ^s	21 ^h 46 ^m 05.6 ^s	+04°23 ^m 02.6 ^s	0.531	4.82	0.436
RXJ2202.7–1902	22 ^h 02 ^m 45.50 ^s	–19°02 ^m 21.1 ^s	22 ^h 02 ^m 45.5 ^s	–19°02 ^m 20.1 ^s	0.438	2.44	0.152
RXJ2328.8+1453	23 ^h 28 ^m 52.27 ^s	+14°52 ^m 42.8 ^s	23 ^h 28 ^m 52.3 ^s	+14°52 ^m 42.7 ^s	0.497	3.88	0.254

^a Coordinates and r_{2500} from [Hoekstra et al. \(2011\)](#).
^b Coordinates from XMM centroid (see Section 4.2).
^c Cluster redshift from [Mullis et al. \(2003\)](#).
^d Column density from [Kalberla et al. \(2005\)](#).

TABLE 2
OBSERVATIONS OF CLUSTERS

Cluster Name	OBSID	Exposure Time (s)	Usable Exposure Time		Time pn
			MOS1	MOS2	
RXJ0056.9–2740	0111282001	8876	8190	8017	4135
RXJ0110.3+1938	0500940101	32818	18883	18497	6973
RXJ0522.2–3625	0065760201	31919	31333	31317	26904
...	0302580901	31110	20077	20284	16481
RXJ0826.1+2625	0691670201 ^a	48742	31516	31419	23135
...	0603500301 ^a	40509	19967	20463	...
RXJ0847.1+3449	0107860501	91419	58708	58333	...
RXJ0957.8+6534	0502430201	72070	44762	45062	30090
RXJ1117.4+0743	0203560401	86515	81073	...	56293
...	0203560201	81913	71366	...	57255
...	0082340101	63206	60889	...	43232
RXJ1354.2–0221	0112250101	33646	24584	24000	...
RXJ1642.6+3935	0603500701 ^a	23917	17108	17133	11099
RXJ2059.9–4245	0691670101 ^a	57915	56794	56571	41238
RXJ2108.8–0516	0110860101	38116	34637	34668	...
RXJ2139.9–4305	0603501001 ^a	41916	36715	36875	19382
RXJ2146.0+0423	0302580701	47120	24091	24081	18316
RXJ2202.7–1902	0203450201	64117	27842	26081	6919
RXJ2328.8+1453	0502430301	104910	94004	94249	70516

^a New data.

TABLE 3
MASKED SOURCES

α_{2000}	δ_{2000}	Radius (")
00 ^h 56 ^m 48.44 ^s	–27°40 ^m 59.5 ^s	12.9
00 ^h 56 ^m 49.65 ^s	–27°40 ^m 07.6 ^s	25.8
00 ^h 57 ^m 04.10 ^s	–27°41 ^m 11.5 ^s	21.5
00 ^h 57 ^m 04.70 ^s	–27°40 ^m 23.5 ^s	21.5
00 ^h 57 ^m 09.22 ^s	–27°39 ^m 39.5 ^s	20.5

NOTE. — Table 3 is published in its entirety in the electronic edition of the *Astrophysical Journal*. A portion is shown here for guidance regarding its form and content.

which the estimated mean mass density is 2500 times the critical density at the redshift of the cluster. Weak

lensing mass measurements used in this work were derived for r_{2500} for each cluster. This radius was typically between 40–60". For background regions, we used annuli centered on the cluster with inner radii of 1.2' and outer radii of 1.8'. We chose to use this size to obtain as local a background on the detector as possible without any detectable cluster emission present. For typical ranges of beta-profile parameters ([Vikhlinin et al. 1998](#)) we estimate that our choice of background annuli may slightly over-subtract the flux at < 1% level, well below our statistical uncertainties. This estimate is conservative because a single beta-model tends to over-predict the X-ray surface brightness when extrapolated to large radii (e.g. [Ettori & Brighenti 2008](#)).

With one exception, when choosing a center for our apertures, we used the Brightest Cluster Galaxy (BCG) coordinates presented in [Hoekstra et al. \(2011\)](#). This

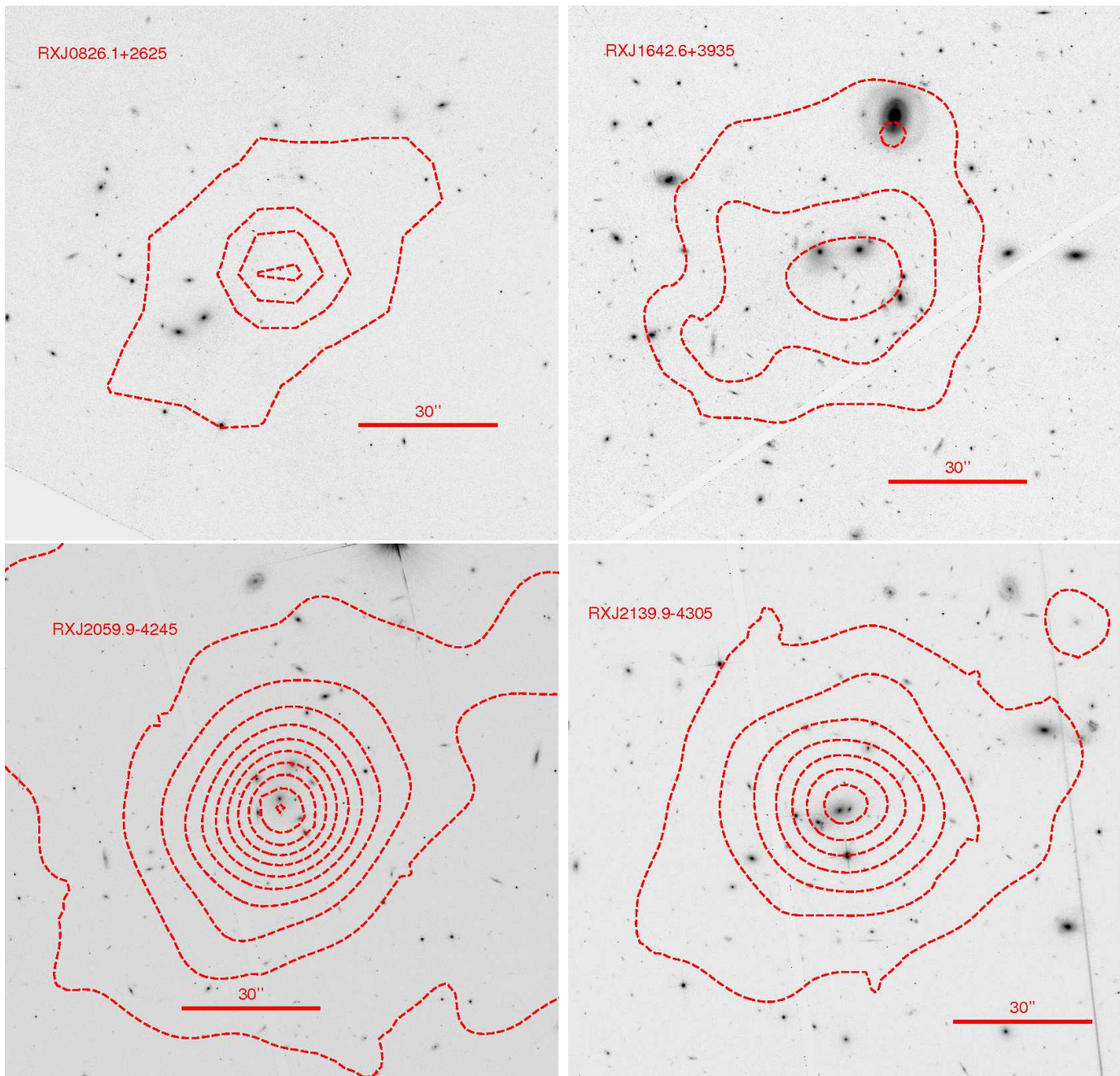


FIG. 1.— Gaussian-smoothed X-ray emission contours overlaid on *Hubble Space Telescope* images of the four clusters we observed in this work. Contours are spaced at intervals of 10^{-6} count s^{-1} arcsec $^{-2}$, with the minimum level for each cluster described in Section 2.

position is the center around which they estimate r_{2500} and M_{2500} , and a direct comparison between the mass and X-ray properties of a cluster should be within the same area. The exception, RXJ0826.1+2625, we will show in Section 4.1, is an example where the *ROSAT* center is in error due to point source contamination. Hoekstra et al. (2011) identified a BCG with a reported “quality” of the BCG detection of 0, implying an ambiguous identification. Furthermore, their reported value of $M_{2500} = 0.8^{+2.1}_{-2.1}$ implies a poor determination of the cluster mass around that location. As the center of the X-ray emission detected in *XMM-Newton* is barely within r_{2500} of the reported BCG position, we instead repositioned our aperture around the center of the X-ray emission.

The coordinates around which we located our apertures are provided in Table 1. Because of the centering issues, RXJ0826.1+2625 was not included in fits of weak-lensing mass scaling relations.

Spectra were extracted using the SAS task `evselect`, while redistribution matrix files (RMF) and ancillary response files (ARF) were generated with SAS tasks `rmfgen` and `arfgen`, respectively. The task `backscale` was used to determine the usable area (correcting for bad pixels and CCD edges) for each spectrum. Photon spectra, RMF, and ARF were all binned from 0.4 to 8.0 keV with bins of size 0.038 keV.

3. ANALYSIS

Our extracted spectra were analyzed using XSPEC version 12.8.0 and PyXspec version 1.0.1. For each cluster, three independent spectra from MOS1, MOS2, and pn were fit simultaneously with the same model. In all three observations of RXJ1117.4+0743, the cluster aperture we chose extended outside of the field of view for the MOS2 camera. As this would bias our results toward the properties of the center of the cluster, we did not use those MOS2 data for any of the three observations. Aside from the spectral binning performed in the spectral generation, no binning was performed. Because of that – and the low number of counts for our objects – we used the modified C-statistic (Cash 1979; Wachter et al. 1979) for determining the best fit and uncertainties for our model parameters.

Our spectra were modeled with a combination of emission (APEC) and absorption (phabs) components from 0.7–8.0 keV. APEC uses the ATOMDB v2.0.2¹² code to compare the observed data to models of collisionally ionized diffuse gas emission spectra. It requires the redshift (from Mullis et al. 2003) and metal abundances to fit a normalization and plasma temperature. We used the `angr` abundance table, which comes from Anders & Grevesse (1989).

For all model fits, we used XSPEC to derive flux values from 0.5–2.0 keV, the same range used by Mullis et al. (2003). We also calculated luminosities from 0.1–2.4 keV (the range presented in Hoekstra et al. 2011), 0.5–2.0 keV (to match Mullis et al. 2003), and 0.1–50 keV (a “bolometric” luminosity).

4. RESULTS

The results of our spectral fitting are summarized in Table 4. Mass estimates based on weak-lensing analyses are those reported in Hoekstra et al. (2011). Our reported luminosities are the unabsorbed luminosities. For all measurements, the reported errors are at the 1σ level.

4.1. Flux

One of our aims was to investigate how improved *XMM-Newton* imaging would affect the measurements of these faint clusters. Along with improved spectral response and calibrations, the improved resolution allowed us to identify and mask out contaminating point sources. To this end, we compare our measured fluxes to those reported in the initial 160SD paper of Vikhlinin et al. (1998), V98 hereafter.

In the original work, V98 were unable to use a wide aperture to integrate flux due to the large statistical uncertainty introduced by the *ROSAT* background. Instead, they estimated the flux from the normalization of a β -model (Cavaliere & Fusco-Femiano 1976),

$$I(r, r_c) = I_0(1 + r^2/r_c^2)^{-3\beta+0.5}. \quad (1)$$

They estimated core radii by fitting a $\beta = 0.67$ model to their surface brightness profiles; then, they extrapolated to obtain the flux based on the normalization and shape of the best-fit β -model. Their final reported flux was actually $(f_{0.6} + f_{0.7})/2$, where $f_{0.6}$ and $f_{0.7}$ are the fluxes obtained assuming $\beta = 0.6$ and $\beta = 0.7$, respectively.

For direct comparison with these results, we integrated counts inside a fixed aperture. In order to avoid biasing

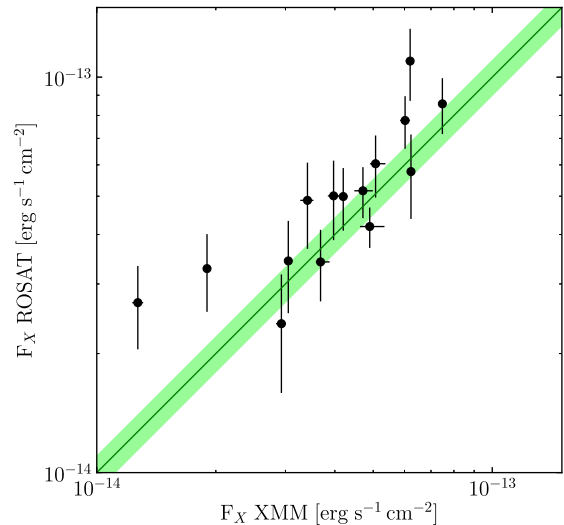


FIG. 2.— Comparison between our measured fluxes using *XMM-Newton* and those reported by Vikhlinin et al. (1998) using *ROSAT*. *ROSAT* fluxes were adjusted to correspond to the inner $300 h_{70}^{-1}$ kpc of the cluster, as described in the text. The solid line is the identity line, while the shaded band indicates agreement to within 10%.

these results by our somewhat uncertain estimation of r_{2500} , we adopted a metric aperture of radius $300 h_{70}^{-1}$ kpc. For the equivalent flux, we used the β -model parameters from V98 to infer the estimated *ROSAT* fluxes inside $300 h_{70}^{-1}$ kpc. The errors on these fluxes were kept at the same percent as the originally reported values. Details of this procedure are given in Appendix A. The comparison between our results and V98 is shown in Figure 2.

Our measured fluxes agree to within 1σ with the modified fluxes of V98 in all but six cases. For RXJ0847.1+3449, including an *XMM-Newton* point source blended with the cluster causes the measured fluxes to agree within their combined 1σ errors. To match our flux measurement of RXJ0056.9–2740 with that of V98, we only needed to center our aperture on the same position. RXJ2146.0+0423, which we find to be slightly lower in flux than allowed by V98’s uncertainty, matches perfectly when we shift to the V98 coordinates and expand the aperture to include a nearby *XMM-Newton* point source. To account for our expanded aperture, we rederived a new, corrected V98 flux to compare in this case. Similarly, repositioning our aperture around RXJ0522.2–3625 and using a larger aperture brings the two measurements into agreement. Finally, RXJ0826.1+2625 and RXJ2328.8+1453 were originally measured at a significant positional offset from V98 ($\approx 37''$ and $45''$, respectively). In both cases, it appears as if the *ROSAT* images blended in nearby point sources. By recentering our aperture around the V98 coordinates and expanding the region to include the neighboring objects, we find agreement between the two sets of flux measurements.

We have reproduced the *ROSAT* X-ray flux estimates from V98 and demonstrated that blended point sources and off-center apertures affected the flux estimates of these clusters over and above the uncertainty based on

¹² <http://atomdb.org/>

TABLE 4
 SPECTRAL FITTING PROPERTIES WITHIN r_{2500}

Name	Mass ^a $h_{70}^{-1} 10^{13}$ M_{\odot}	kT keV	Abundance Z_{\odot}	Norm. 10^{-4} APEC ^e	F ^b 10^{-14} $\text{erg s}^{-1} \text{cm}^{-2}$	L ^c $h_{70}^{-2} 10^{44}$ erg s^{-1}	L ^b $h_{70}^{-2} 10^{44}$ erg s^{-1}	L ^d $h_{70}^{-2} 10^{44}$ erg s^{-1}
RXJ0056.9–2740	$5.2^{+4.2}_{-3.0}$	$3.51^{+0.91}_{-0.49}$	$< 1.03^f$	$1.97^{+0.16}_{-0.19}$	$4.59^{+0.26}_{-0.36}$	$0.524^{+0.044}_{-0.032}$	$0.437^{+0.036}_{-0.031}$	$1.05^{+0.08}_{-0.10}$
RXJ0110.3+1938	$5.0^{+3.4}_{-2.6}$	$2.95^{+0.72}_{-0.62}$	$0.56^{+0.50}_{-0.32}$	$0.98^{+0.19}_{-0.16}$	$3.64^{+0.20}_{-0.08}$	$0.119^{+0.003}_{-0.006}$	$0.102^{+0.002}_{-0.006}$	$0.219^{+0.016}_{-0.015}$
RXJ0522.2–3625	$7.2^{+4.2}_{-3.1}$	$5.32^{+0.42}_{-0.37}$	$0.37^{+0.13}_{-0.12}$	$2.11^{+0.08}_{-0.09}$	$6.11^{+0.13}_{-0.10}$	$0.454^{+0.012}_{-0.012}$	$0.371^{+0.010}_{-0.009}$	$1.19^{+0.04}_{-0.03}$
RXJ0826.1+2625	$0.8^{+2.1}_{-2.1}$	$1.52^{+0.20}_{-0.27}$	$0.13^{+0.12}_{-0.08}$	$0.31^{+0.06}_{-0.05}$	$0.80^{+0.05}_{-0.02}$	$0.035^{+0.002}_{-0.002}$	$0.031^{+0.001}_{-0.002}$	$0.045^{+0.002}_{-0.003}$
RXJ0847.1+3449	$24.2^{+8.9}_{-7.6}$	$4.17^{+0.59}_{-0.40}$	$0.29^{+0.18}_{-0.16}$	$2.02^{+0.13}_{-0.13}$	$5.20^{+0.11}_{-0.10}$	$0.568^{+0.012}_{-0.012}$	$0.467^{+0.009}_{-0.009}$	$1.31^{+0.03}_{-0.05}$
RXJ0957.8+6534	$4.3^{+3.2}_{-2.6}$	$2.88^{+0.21}_{-0.17}$	$0.23^{+0.10}_{-0.08}$	$1.65^{+0.09}_{-0.09}$	$3.95^{+0.09}_{-0.07}$	$0.393^{+0.009}_{-0.011}$	$0.330^{+0.009}_{-0.009}$	$0.745^{+0.012}_{-0.019}$
RXJ1117.4+0743	$5.2^{+3.4}_{-2.8}$	$4.31^{+0.69}_{-0.39}$	$0.40^{+0.19}_{-0.19}$	$1.01^{+0.07}_{-0.06}$	$2.90^{+0.06}_{-0.04}$	$0.224^{+0.004}_{-0.004}$	$0.184^{+0.004}_{-0.003}$	$0.527^{+0.012}_{-0.015}$
RXJ1354.2–0221	$20.2^{+6.4}_{-5.6}$	$7.55^{+1.86}_{-1.21}$	$0.38^{+0.34}_{-0.27}$	$2.55^{+0.18}_{-0.19}$	$6.89^{+0.25}_{-0.19}$	$0.679^{+0.025}_{-0.020}$	$0.547^{+0.021}_{-0.024}$	$2.12^{+0.09}_{-0.09}$
RXJ1642.6+3935	$2.8^{+2.8}_{-1.8}$	$3.01^{+0.41}_{-0.38}$	$0.43^{+0.26}_{-0.20}$	$0.95^{+0.10}_{-0.10}$	$3.43^{+0.16}_{-0.08}$	$0.147^{+0.005}_{-0.006}$	$0.127^{+0.004}_{-0.005}$	$0.264^{+0.011}_{-0.012}$
RXJ2059.9–4245	$4.4^{+3.3}_{-2.4}$	$2.58^{+0.10}_{-0.10}$	$0.53^{+0.10}_{-0.08}$	$1.93^{+0.09}_{-0.09}$	$7.25^{+0.12}_{-0.09}$	$0.250^{+0.003}_{-0.005}$	$0.216^{+0.004}_{-0.004}$	$0.424^{+0.007}_{-0.008}$
RXJ2108.8–0516	$1.8^{+2.2}_{-1.4}$	$2.34^{+0.90}_{-0.49}$	$< 2.67^f$	$1.16^{+0.10}_{-0.29}$	$2.89^{+0.13}_{-0.32}$	$0.097^{+0.009}_{-0.008}$	$0.082^{+0.009}_{-0.003}$	$0.161^{+0.018}_{-0.014}$
RXJ2139.9–4305	$5.3^{+3.7}_{-2.6}$	$3.06^{+0.23}_{-0.22}$	$0.32^{+0.12}_{-0.10}$	$1.86^{+0.10}_{-0.10}$	$6.13^{+0.11}_{-0.16}$	$0.297^{+0.006}_{-0.008}$	$0.255^{+0.005}_{-0.006}$	$0.542^{+0.010}_{-0.013}$
RXJ2146.0+0423	$21.0^{+6.7}_{-5.7}$	$5.02^{+0.41}_{-0.38}$	$0.41^{+0.14}_{-0.12}$	$2.98^{+0.13}_{-0.13}$	$7.87^{+0.18}_{-0.17}$	$0.739^{+0.017}_{-0.021}$	$0.601^{+0.018}_{-0.020}$	$1.97^{+0.06}_{-0.04}$
RXJ2202.7–1902	$0.8^{+2.0}_{-0.8}$	$3.91^{+0.79}_{-0.63}$	$0.77^{+0.59}_{-0.39}$	$0.37^{+0.06}_{-0.06}$	$1.29^{+0.07}_{-0.04}$	$0.084^{+0.005}_{-0.005}$	$0.071^{+0.004}_{-0.005}$	$0.186^{+0.008}_{-0.012}$
RXJ2328.8+1453	$4.0^{+3.7}_{-2.6}$	$3.12^{+0.28}_{-0.23}$	$0.38^{+0.16}_{-0.12}$	$0.59^{+0.04}_{-0.04}$	$1.58^{+0.04}_{-0.02}$	$0.135^{+0.003}_{-0.003}$	$0.113^{+0.003}_{-0.003}$	$0.269^{+0.007}_{-0.005}$

^a Weak lensing masses from [Hoekstra et al. \(2011\)](#).

^b 0.5 - 2.0 keV.

^c 0.1 - 2.4 keV.

^d Bolometric.

^e $10^{-14} (4\pi[D_A(1+z)]^2)^{-1} \int n_e n_H dV$. D_A has units cm. n_e and n_H have units cm^{-3} .

^f 3σ upper limit.

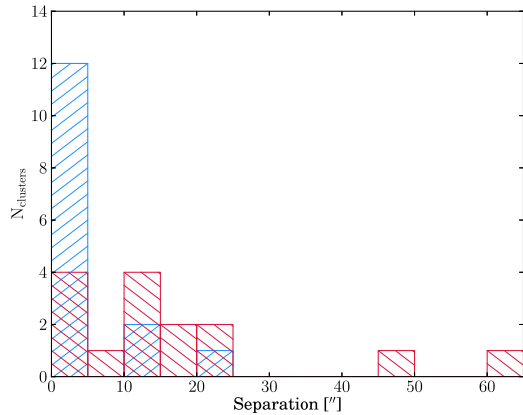


FIG. 3.— Distribution of X-ray centroid offsets to BCG positions measured by [Hoekstra et al. \(2011\)](#) using *XMM-Newton* (this work, hashes rising to the right) and *ROSAT* ([Vikhlinin et al. 1998](#), hashes lowering to the right). Data are binned to increments of 5 arcseconds.

counting statistics and background subtraction alone.

4.2. X-ray Offsets

In Table 1 we list coordinates for each cluster twice. The coordinates from [Hoekstra et al. \(2011\)](#) are their best estimate of the position of each cluster’s BCG. The new coordinates are of an X-ray centroid performed on data from the MOS1 camera around each cluster’s X-ray emission. Centroids were computed in five iterations of centroiding an aperture with radius $16''$, of images binned to $1.6''$ per pixel. Twelve of the X-ray-determined positions are within $5''$ of the BCG position, and the only position more than $12''$ from the BCG is for RXJ0826.1+2625, where the BCG identification may

be questionable. We plot our results, along with the offsets using X-ray positions from *ROSAT*, in Figure 3. These *XMM-Newton* observations provide a significant improvement in the ability to properly detect the cluster position over the original *ROSAT* detection positions.

4.3. Scaling Relations

We fit our measurements of bolometric luminosity, temperature, and mass inside r_{2500} to the relation

$$\log\left(\frac{Y}{Y_0}\right) = \alpha \log\left(\frac{X}{X_0}\right) + C_X. \quad (2)$$

X_0 and Y_0 are pivot values, which were $10^{44} \text{ erg s}^{-1}$, 4 keV, and $10^{14} M_{\odot}$ for luminosity, temperature, and mass, respectively. Luminosity and mass were corrected for redshift evolution by including the factor $E(z)$; fits were therefore of $L/E(z)$ and $ME(z)$. To extend the dynamic range of our sample and to compare our low mass sample with a higher mass sample at similar redshift, we also included data from the Canadian Cluster Comparison Project ([Hoekstra et al. 2012](#); [Mahdavi et al. 2013](#), hereafter CCCP). This sample of 50 galaxy clusters spans redshifts $0.15 < z < 0.55$, and all clusters were required to have a temperature $k_B T_X > 3$ keV. CCCP data was acquired through the online database¹³. In an erratum ([Mahdavi et al. 2014](#)) these data have been updated since original publication to fix an error in the bolometric luminosity correction factor. We therefore present all of the cluster properties used for fitting in Table 5; a full table is provided in the online edition.

Individual fits are discussed below, but the results are given in Table 6. Fits including data in this work

¹³ <http://sfstar.sfsu.edu/cccp>

TABLE 5
CCCP CLUSTER PROPERTIES WITHIN r_{2500}

Name	Mass \times E(z) $h_{70}^{-1} 10^{14} M_{\odot}$	L/E(z) $h_{70}^{-2} 10^{45} \text{ erg s}^{-1}$	kT keV	Redshift
3C295	3.30 ± 0.86	0.78 ± 0.01	6.43 ± 0.35	0.464
Abell0068	2.87 ± 0.645	0.96 ± 0.02	7.25 ± 0.34	0.255
Abell0115N	0.68 ± 0.46	0.47 ± 0.01	4.84 ± 0.10	0.197
Abell0115S	0.84 ± 0.53	0.32 ± 0.01	5.60 ± 0.24	0.197
Abell0209	2.05 ± 0.43	0.97 ± 0.01	7.14 ± 0.34	0.206

NOTE. — Table 5 is published in its entirety in the electronic edition of the *Astrophysical Journal*. A portion is shown here for guidance regarding its form and content.

TABLE 6
SCALING RELATIONS

X	Y	Sample	Log Slope	Log Intercept	Bootstrapped	Notes
L/E(z)	ME(z)	CCCP+160SD	0.305 ± 0.042	0.134 ± 0.043	NO	WLS, $\sigma_{\log(M L)} = 0.100$
L/E(z)	ME(z)	CCCP+160SD	0.435 ± 0.047	-0.039 ± 0.049	YES	BCES(Y X)
L/E(z)	ME(z)	CCCP	0.291 ± 0.075	0.135 ± 0.082	YES	WLS, $\sigma_{\log(M L)} = 0.137 \pm 0.028$
L/E(z)	ME(z)	CCCP	0.379 ± 0.081	0.005 ± 0.091	YES	BCES(Y X)
L/E(z)	ME(z)	160SD	1.02 ± 0.17	0.195 ± 0.076	YES	BCES(Y X)
ME(z)	L/E(z)	CCCP+160SD	2.33 ± 0.27	0.079 ± 0.111	YES	BCES(X Y)
ME(z)	L/E(z)	CCCP	2.78 ± 0.73	-0.071 ± 0.311	YES	BCES(X Y)
ME(z)	L/E(z)	160SD	1.01 ± 0.225	-0.186 ± 0.066	YES	BCES(X Y)
L/E(z)	T	CCCP+160SD	0.229 ± 0.016	0.005 ± 0.015	YES	WLS, $\sigma_{\log(T L)} = 0.073 \pm 0.009$
L/E(z)	T	CCCP+160SD	0.225 ± 0.016	0.012 ± 0.015	YES	BCES(Y X)
L/E(z)	T	CCCP	0.257 ± 0.029	-0.026 ± 0.029	YES	WLS, $\sigma_{\log(T L)} = 0.070 \pm 0.009$
L/E(z)	T	CCCP	0.261 ± 0.029	-0.028 ± 0.028	YES	BCES(Y X)
L/E(z)	T	160SD	0.300 ± 0.055	0.052 ± 0.030	NO	WLS, $\sigma_{\log(T L)} = 0.066$
L/E(z)	T	160SD	0.293 ± 0.064	0.063 ± 0.039	YES	BCES(Y X)
T	L/E(z)	CCCP+160SD	4.47 ± 0.33	-0.057 ± 0.072	YES	BCES(X Y)
T	L/E(z)	CCCP	3.88 ± 0.45	0.098 ± 0.100	YES	BCES(X Y)
T	L/E(z)	160SD	3.29 ± 0.57	-0.225 ± 0.090	NO	BCES(X Y)
T	ME(z)	CCCP+160SD	1.88 ± 0.21	-0.058 ± 0.049	YES	BCES Bisector
T	ME(z)	CCCP+160SD	1.93 ± 0.24	-0.066 ± 0.053	YES	BCES Orthogonal
T	ME(z)	CCCP	1.65 ± 0.24	-0.005 ± 0.061	YES	BCES Bisector
T	ME(z)	CCCP	1.80 ± 0.33	-0.029 ± 0.077	YES	BCES Orthogonal
T	ME(z)	160SD	1.98 ± 0.92	-0.096 ± 0.100	NO	BCES Bisector
T	ME(z)	160SD	1.79 ± 0.96	-0.103 ± 0.101	NO	BCES Orthogonal
ME(z)	T	CCCP+160SD	0.537 ± 0.059	0.029 ± 0.024	YES	BCES Bisector
ME(z)	T	CCCP+160SD	0.525 ± 0.065	0.032 ± 0.024	YES	BCES Orthogonal
ME(z)	T	CCCP	0.622 ± 0.097	-0.008 ± 0.040	YES	BCES Bisector
ME(z)	T	CCCP	0.574 ± 0.111	0.009 ± 0.044	YES	BCES Orthogonal
ME(z)	T	160SD	0.506 ± 0.235	0.049 ± 0.066	NO	BCES Bisector
ME(z)	T	160SD	0.559 ± 0.300	0.058 ± 0.079	NO	BCES Orthogonal

are labeled “160SD,” while those including CCCP data are marked as such. Except where noted, uncertainties in fit values were derived through 50,000 bootstrap resamplings. Fits were performed using the WLS and BCES methods described by Akritas & Bershady (1996). Where luminosity was serving as the X variable, we used the WLS and BCES (Y|X) methods, which minimized the residuals in the other parameter. Conversely, when luminosity was the Y variable, we used the BCES (X|Y) method. When fitting the mass-temperature relation, we used the BCES Bisector and Orthogonal methods, which considers the residuals in both variables. To account for asymmetric error bars, we estimated a single, logarithmic error for a value X_{-d}^{+u} to be

$$\sigma = 0.4343 \frac{0.5(u+d)}{X}. \quad (3)$$

For clarity, when describing a relation fit by Equation (2), we call it the Y-X relation, where X is the independent variable.

Our first fit was of the luminosity-mass relation within r_{2500} . When fitting this relation, we did not include RXJ0826.1+2625, as its mass was not well determined (as discussed in Section 2). We first fit this relationship without assuming intrinsic scatter; the resulting best-fit slope was $\alpha = 0.435 \pm 0.047$. This result shows no significant difference from the result for the 50 CCCP clusters alone, but it does not agree with the result for a fit only of the low-mass sample presented here. We caution that this discrepancy is not necessarily indicative of a break in the scaling relation, for reasons we will discuss in Section 5.

When allowing for intrinsic scatter, the best-fit value of α is 0.305 ± 0.042 , with an intrinsic scatter of $\sigma_{\log(M|L)} = 0.100$. Figure 4 shows both fits along with the cluster properties for both samples. For a direct comparison of the reduced scatter, we fit the M-L relation using luminosities from the original work by Hoekstra et al. (2011). With these, the intrinsic scatter was $\sigma_{\log(M|L)} = 0.262$.

Next we fit the temperature-luminosity relation within

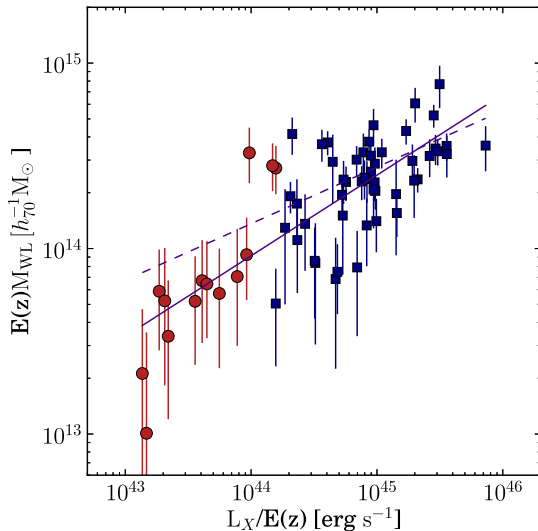


FIG. 4.— Plot of M_{WL} as a function of bolometric X-ray luminosity within r_{2500} . Masses and luminosities have been rescaled by $E(z)$ to account for the range of redshift covered by the samples. Data analyzed in this work are shown as circles, while cluster properties from the CCCP are shown as squares. RXJ0826.1+2625 was not included in this fit. Our best fit to Equation (2) for the M-L relation is shown by the solid line. Our best fit when including intrinsic scatter is shown by the dashed line.

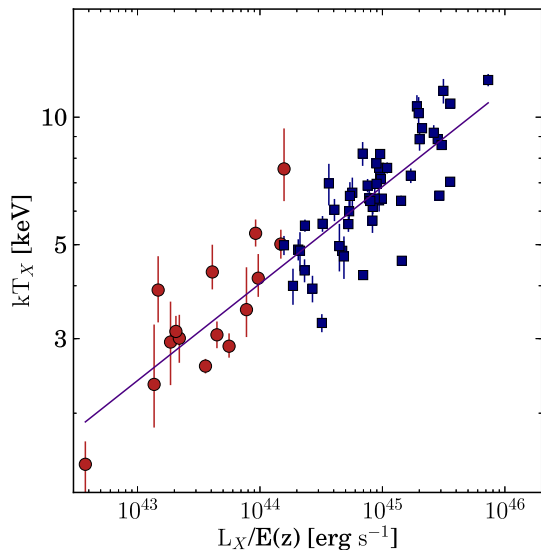


FIG. 5.— Plot of X-ray temperature as a function of bolometric luminosity within r_{2500} . Luminosities have been rescaled by $E(z)$ to account for the range of redshift covered by the samples. Data analyzed in this work are shown as circles, while cluster properties from the CCCP are shown as squares. Our best fit to Equation (2) for the T-L relation is shown by the solid line.

r_{2500} , this time using all fifteen clusters studied here. We found that the best fit for the entire sample was $\alpha = 0.229 \pm 0.016$ with an intrinsic scatter of $\sigma_{\log(T|L)} = 0.073 \pm 0.009$, consistent with the fits for the two individual samples. This fit is shown along with the data in Figure 5. When we did not allow for intrinsic scatter, we found the best-fit slope was relatively unchanged, becoming $\alpha = 0.225 \pm 0.016$.

We also investigated the scaling between mass and temperature within r_{2500} . Again, RXJ0826.1+2625 was

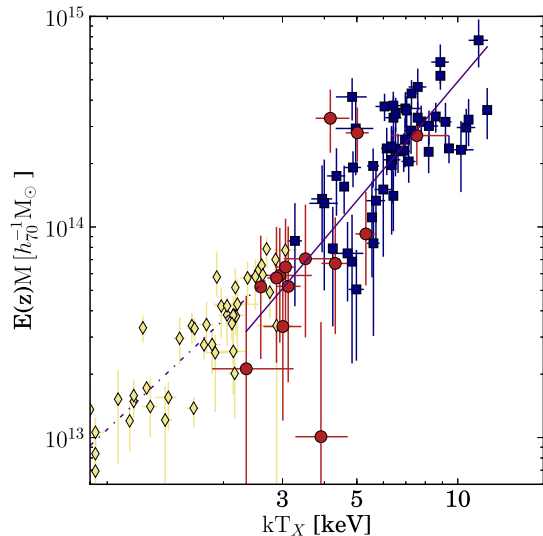


FIG. 6.— Plot of M as a function of X-ray temperature within r_{2500} . Masses have been rescaled by $E(z)$ to account for the range of redshift covered by the samples. Data analyzed in this work are shown as circles, while cluster properties from the CCCP are shown as squares; both are derived from weak lensing. RXJ0826.1+2625 was not included in this fit. We also include a sample of nearby galaxy groups from Sun et al. (2009) as diamonds, where masses are derived from hydrostatic equilibrium. Our best fit to Equation (2) for the M-T relation from the clusters analyzed in this work and from the CCCP is shown by the solid line. Our best fit to the M-T relation using the properties within r_{2500} of the groups from Sun et al. is shown as a dashed line.

excluded from this fit. For the combined sample, the best-fit with the BCES Bisector was $\alpha = 1.88 \pm 0.21$, which was consistent with fits for the sub-samples alone. This fit is shown in Figure 6. In addition, we include data taken from Sun et al. (2009). Masses from that study are not based on weak lensing measurements, but were instead derived from an assumption of hydrostatic equilibrium. These data were not included in our fits, however.

In order to more easily compare our work to other studies, we also fit the inverse of these three relations. Using BCES(X|Y), the L-M relation fit for the CCCP+160SD sample is $\alpha = 2.33 \pm 0.27$. In contrast, for BCES(Y|X), the inverse of the M-L relation is $\alpha^{-1} = 2.30$. Our BCES(Y|X) fit of L-T is $\alpha = 4.47 \pm 0.33$, while the corresponding fit from the T-L relation is $\alpha^{-1} = 4.36$. When fitting T-M, the best fit from BCES Bisector was $\alpha = 0.537 \pm 0.059$, which agrees with the BCES Bisector of M-T, $\alpha^{-1} = 0.532$.

5. DISCUSSION

5.1. Comparison with Previous X-ray Observations

We compared our results to previously published individual *XMM-Newton* results for four clusters (RXJ 0110.3+1938, RXJ0847.1+3449, RXJ1117.4+0743, and RXJ1354.2–0221). To investigate the differences, we replicated the analysis of previous observations, including their aperture sizes and cosmology. We were able to reasonably reproduce previous results. The discrepancies arising from systematics such as differences in background choices or particle background screening criteria are smaller than the statistical uncertainty. We find that any apparent differences between our results for these

clusters with previous results arise because of differences in aperture sizes, and rarely, choice of aperture centers. The details of this comparison are reported in Appendix B.

Our most obvious source of possible discrepancy with previous works is our choice of apertures, which have a radius r_{2500} motivated by weak-lensing estimates from [Hoekstra et al. \(2011\)](#) that were unavailable to most of the other studies. Another potential source of X-ray temperature discrepancy is the choice of binning spectral data. Some previous works binned spectral data to as few as 12 counts per spectral bin. We leave our spectra unbinned and fit with the C-statistic. As this work is focusing on faint clusters, we are limited by low photon counts. If data are binned such that only a few counts are in each bin, each bin will have non-Gaussian behavior. Since the χ^2 statistic is defined for Gaussian-distributed data, it will not be a valid fitting statistic in this case. Alternatively, data can be binned, but doing so potentially degrades spectral resolution. Along with producing better fits for low counts ([Nousek & Shue 1989](#); [Tozzi et al. 2006](#)), use of the C-statistic can also avoid biases in the high-count regime ([Humphrey et al. 2009](#)). Use of different thermal models for fitting spectra did not cause major deviations in our results. As we were able to reproduce the earlier results while still using an APEC model, this should not therefore bias our results significantly (see also [Belsole et al. 2005](#); [Matsushita et al. 2007](#)).

We demonstrated in detail (see Appendix B) that we can recover results of previous works, which verifies their results and ours. However we caution that the choice of aperture and center affect the estimate of L, T, and M for any cluster, and that results from different analyses cannot be blindly combined.

5.2. Comparison with Other Scaling Relations

We have measured scaling relations between weak lensing mass, X-ray luminosity, and temperature for a sample of clusters with mass and luminosity around the cluster/group boundary and at redshifts $0.3 < z < 0.6$. As we used weak lensing masses and bolometric luminosities and because we only investigated X-ray properties within r_{2500} , no exact comparisons are available for our results. However, we can compare our results to other similar studies, both those focused on local groups and those that include clusters at redshifts similar to what was studied here but more massive than our sample.

Our best fit of the M-L relation within r_{2500} was, when neglecting intrinsic scatter, $\alpha = 0.435 \pm 0.047$. [Hoekstra et al. \(2011\)](#) fit this relation using almost the same clusters studied here, with *ROSAT* luminosities taken from the *ROSAT* measurements, and a higher mass sample, reporting $\alpha = 0.68 \pm 0.07$. Other works ([Maughan 2007](#); [Rykoff et al. 2008](#); [Eckmiller et al. 2011](#); [Reichert et al. 2011](#)) find values in the range $0.5 \lesssim \alpha \lesssim 0.75$, consistent with but somewhat steeper than ours.

For the L-T relation within r_{2500} , we found a best fit of $\alpha = 4.47 \pm 0.33$, although the 160SD groups and the CCCP clusters each had shallower slopes when fit independently. Previous results ([Maughan 2007](#); [Pratt et al. 2009](#); [Bruch et al. 2010](#); [Eckmiller et al. 2011](#); [Reichert et al. 2011](#); [Nastasi et al. 2014](#)) have reported slopes from $2.5 \lesssim \alpha \lesssim 4.5$. Our results, particularly for the two sub-samples fit individually, are consis-

tent with this range, albeit on the high end.

In this work, we reported the best fit slope of the M-T relation within r_{2500} was $\alpha = 1.88 \pm 0.21$. Previous works ([Sun et al. 2009](#); [Eckmiller et al. 2011](#); [Reichert et al. 2011](#); [Kettula et al. 2013](#)) have reported slopes in the range $1.45 \lesssim \alpha \lesssim 1.85$. As was the case with the T-L relation, our slope for the combined sample is slightly higher than this range, but the group and cluster samples, when fit independently, are both in agreement with these studies.

While comparing our scaling relationships to others is worthwhile, we caution that there are a handful of issues that make direct comparison problematic. As mentioned earlier in this discussion, other works used different radii within which to measure cluster properties. Our choice of r_{2500} was motivated by the requirements imposed from our weak lensing masses, but it means we are analyzing X-ray properties in different apertures from other studies.

Another issue that arises when comparing to other studies is the definition of luminosity. In this work, we used bolometric luminosities. However, in the three works that looked at groups that we discuss in this section ([Rykoff et al. 2008](#); [Hoekstra et al. 2011](#); [Eckmiller et al. 2011](#)), all fit scaling relations with a luminosity only within the energy band of 0.1 - 2.4 keV. The importance of energy bands was shown by [Markevitch \(1998\)](#), who found that when switching from luminosities within 0.1-2.4 keV to bolometric luminosities the measured slope of the L-T relation steepened from $\alpha = 2.10 \pm 0.24$ to $\alpha = 2.64 \pm 0.27$. Such a large change in the fit means that we should be careful comparing scaling relations for luminosities derived from different energy bands. As a test of this effect, we fit the M-L and T-L relations using luminosities measured in the 0.1 - 2.4 keV energy band for the 160SD clusters. The power law indices increased when using the energy limited luminosities from 1.02 ± 0.17 to $\alpha = 1.19 \pm 0.22$ and from 0.293 ± 0.064 to $\alpha = 0.334 \pm 0.101$ for M-L and T-L, respectively. The 160SD sample here has too small a dynamical range to be seriously considered for a scaling relation, but the effect of choosing to fit bolometric luminosities over band-limited luminosities is clear.

Also, while our sample is a subset of a randomly selected survey, it is originally based on X-ray selected clusters. [Hicks et al. \(2013\)](#) suggest that X-ray selection preferentially picks centrally concentrated systems; these systems populate the high L_X side of the T-L relation. Similarly, since our data were drawn from the faint end of a flux-limited sample, we would expect preferentially over-luminous clusters for their mass to be selected.

5.3. Comparison to Low-Redshift Groups

One of the issues with comparing the difference between the groups examined in this paper and those at low redshift is the ubiquity of masses derived from hydrostatic equilibrium. Hydrostatic masses may somewhat underestimate the mass of galaxy clusters when compared to weak lensing measurements ([Arnaud et al. 2007](#); [Mahdavi et al. 2008, 2013](#)). However, in order to allow a comparison with work on low redshift groups and poor clusters using hydrostatic masses, we make the assumption that both mass estimates are identical.

Looking at Figure 6, we can see that our moderate red-

shift clusters ($\bar{z} = 0.444$) are almost all hotter and/or less massive than what would be predicted by the lower redshift scaling relations for groups presented in Sun et al. (2009) ($\bar{z} = 0.042$), although five low-temperature clusters agree very well. If we test the hypothesis whether our data are fit by the Sun2009 relationship between mass and temperature, we find a χ^2 value of 19.09 for 14 clusters ($p = 0.089$). Therefore, to within $2 - \sigma$ we see no difference between our sample and the low-redshift sample. If we limit this analysis to only those clusters with temperature $kT < 4$ keV, our value of χ^2 is 3.15 for 9 clusters ($p = 0.87$). If we do not scale the mass by $E(z)$, χ^2 becomes 29.53 for 14 clusters ($p = 0.0033$). This significance is just below 3σ , constituting very weak evidence for the expected self-similar evolution in the temperature-mass relation for groups.

5.4. Comparison between Groups and Clusters

A direct comparison between the CCCP sample and our sample, which affords a comparison between low-mass and high-mass clusters at a similar redshift range, is difficult due to the limited number of clusters in both sets. So to provide some quantification of whether the two populations differ, we utilize Fisher's exact test, which looks at how two properties are distributed in two populations. In this case, we look at how our sample and the CCCP sample compare to the scaling relations. We choose to use Fisher's exact test due to how few objects we have; in this domain, Fisher's exact test is the best, if not the only, test to use (Wall & Jenkins 2012).

For both samples, we count how many clusters lie above the lines of best fit for each scaling relation and how many lie below. Our null hypothesis is that the samples are similar and so the number of clusters above the relation should equal the number below, statistically. We compute p-values for the T-L, M-L, and M-T relations of $p = 0.13$, $p = 0.19$, and $p = 0.19$, respectively. We therefore cannot reject the hypothesis that groups and clusters at intermediate redshift behave identically with respect to the scaling relations derived in this work, so our measurements are consistent with the hypothesis that $z \sim 0.3-0.5$ X-ray selected clusters and groups/poor clusters follow similar X-ray scaling laws.

6. CONCLUSIONS

We have presented new and revised X-ray properties for a sample of 15 galaxy clusters originally drawn from a random sample of the 160 Square Degree Survey. Covering a range of redshifts from $0.3 < z < 0.6$ and limited in mass to $M_{2500} \lesssim 2 \times 10^{15} M_{\odot}$, our new X-ray data together with previously published HST weak lensing measurements probe a largely-unexplored parameter space in cluster mass and redshift. By using a rigorous analysis to match cluster properties measured within the same radius as existing weak-lensing masses, we investigate scaling relations between mass, luminosity, and temperature. Our primary conclusions are summarized below.

1. We measure fainter fluxes than reported from earlier *ROSAT* measurements (Vikhlinin et al. 1998) for five of the fifteen clusters studied here (RXJ0522.2-3625, RXJ0826.1+2625, RXJ0847.1+3449, RXJ2146.0+0423, RXJ2328.8+1453). Due to a combination of fainter sources blending into the extended cluster light profile

and multiple sources blending into one, we also found that reported X-ray positions for these clusters were not accurate. Due to the original positional inaccuracy, RXJ0056.9-2740 was originally reported to be fainter than we measured. Use of detections near the flux threshold of objects subject to blending because of the angular resolution, such as *ROSAT* cluster surveys, can therefore lead to errors in both position and flux that can be larger than the quoted statistical flux uncertainty.

2. Inside r_{2500} , for the mass and redshift range studied here, the fourteen clusters with reasonable mass measurements and 50 clusters from the CCCP are best fit by the relation

$$\frac{ME(z)}{10^{14} M_{\odot}} = 10^{-0.04 \pm 0.05} \times \left(\frac{LE(z)^{-1}}{10^{44} \text{ erg s}^{-1}} \right)^{0.44 \pm 0.05} \quad (4)$$

When we allow for intrinsic scatter, the exponent of the best fit becomes 0.31 ± 0.04 . Our results indicate neither a break in the scaling relation among groups nor increased scatter at low mass.

3. Using uncontaminated luminosity measurements and uniformly-defined r_{2500} values from weak lensing, the intrinsic scatter in the L-M relation reduced from $\sigma_{\log(M|L)} = 0.26$ to $\sigma_{\log(M|L)} = 0.10$.

4. Similarly, when determining the scaling relation between luminosity and temperature within r_{2500} , we find that

$$\frac{k_B T}{4 \text{ keV}} = 10^{0.005 \pm 0.015} \times \left(\frac{LE(z)^{-1}}{10^{44} \text{ erg s}^{-1}} \right)^{0.23 \pm 0.02} \quad (5)$$

We find a small intrinsic scatter of $\sigma_{\log(T|L)} = 0.07 \pm 0.01$. When the high- and low-mass samples are fit separately, the 50 clusters from the CCCP sample and the 15 clusters from the 160SD sample scaling relations each have steeper slopes, 0.26 ± 0.03 and 0.30 ± 0.06 , respectively. Again, we find no evidence of a break in this relation among groups.

5. For scaling between weak-lensing masses and X-ray temperatures within r_{2500} , the combined sample of 14 clusters from this work with reasonable mass measurements and 50 from the CCCP are best fit by the relation

$$\frac{ME(z)}{10^{14} M_{\odot}} = 10^{-0.06 \pm 0.05} \times \left(\frac{k_B T}{4 \text{ keV}} \right)^{1.9 \pm 0.2} \quad (6)$$

When fitting high and low mass subsamples independently, the slope becomes 1.7 ± 0.2 and 1.8 ± 1.0 , respectively. These results agree with other results for both nearby groups and intermediate-redshift clusters, along with the self-similar prediction that $M \propto T^{3/2}$.

6. To the statistical limits of our data, the intermediate redshift groups are within 2σ of the M-T relation extrapolated from a low-redshift group sample from Sun et al. (2009). Without self-similar evolution, there is a deviation just below the level of 3σ , indicating a weak statistical preference for the expected self-similar evolution.

The authors wish to thank Seth Bruch for his work planning this project. M.D. and T.C. acknowledge partial support from a NASA ADAP award NNX11AJ60G. A.M. acknowledges support from NASA

grant NNX12AE45G. This work is based on observations obtained with *XMM-Newton*, an ESA science mission

with instruments and contributions directly funded by ESA Member States and NASA.

Facility: XMM

APPENDIX

CONVERSION OF ROSAT FLUXES TO $F_{300\text{KPC}}$

In this appendix, we discuss how we converted the fluxes reported by [Vikhlinin et al. \(1998\)](#) into aperture fluxes. As the original fluxes were found by integrating a β -model to infinity, we derived a means of obtaining the normalization from a given flux. We then integrated the β -model to a desired angular aperture using this normalization.

The flux of a β -model is found by integrating the intensity

$$f = \int I_0 \left(1 + \left(\frac{\theta}{\theta_c} \right)^2 \right)^{-3\beta+0.5} 2\pi\theta d\theta. \tag{A1}$$

Substituting $x = -3\beta + 0.5$, this is an analytic integral with solution

$$f = 2\pi I_0 \frac{(\theta_c^2 + \theta^2)(\theta^2/\theta_c^2 + 1)^x}{2(x + 1)} + c \tag{A2}$$

When evaluating this as $\theta \rightarrow \infty$ for any $x < 1$, the upper part of the fraction will go to 0. When evaluating at $\theta = 0$, this becomes

$$f(\theta = 0) = 2\pi I_0 \frac{\theta_c^2}{2(x + 1)}. \tag{A3}$$

As [Vikhlinin et al. \(1998\)](#) reported their fluxes as the average of the fluxes found with $\beta = 0.6$ and $\beta = 0.7$, we can determine their normalization, I_0 , by inserting the appropriate values of x and rearranging Equation (A3). We use $x_{0.6}$ and $x_{0.7}$ to denote the values of x found with $\beta = 0.6$ and $\beta = 0.7$, respectively, and include a factor of 1/2 to account for averaging, so that we have

$$I_0 = \frac{-2f_{ROSAT}}{\pi\theta_c^2} \left(\frac{1}{x_{0.6} + 1} + \frac{1}{x_{0.7} + 1} \right)^{-1}. \tag{A4}$$

From this, the total flux that would be measured inside a aperture of radius θ can be computed for a given value of β using

$$f_x(\theta) = \frac{-2f_{ROSAT}}{\theta_c^2(x + 1)} \left(\frac{1}{x_{0.6} + 1} + \frac{1}{x_{0.7} + 1} \right)^{-1} \left[(\theta_c^2 + \theta^2) \left(\frac{\theta^2}{\theta_c^2} + 1 \right)^x - \theta_c^2 \right]. \tag{A5}$$

To compare the *ROSAT* fluxes to our own, we solve this for the angle equivalent to 300 kpc for $\beta = 0.6$ and $\beta = 0.7$, averaging the two results.

REPLICATION OF PREVIOUS XMM ANALYSES

RXJ0110.3+1938

[Bruch et al. \(2010\)](#) first analyzed this cluster with the same observation used in this paper. While their analysis followed a similar path to our own, their reported results are not the same as ours. Our reported bolometric luminosity is similar to theirs ($2.19_{-0.14}^{+0.12}$ and $2.08_{-0.22}^{+0.22} \times 10^{43}$ erg s⁻¹, respectively), but their reported temperature is noticeably lower than our own ($1.46_{-0.19}^{+0.26}$ keV compared to $2.95_{-0.62}^{+0.72}$ keV). The difference in the result may arise from their less stringent cut for selecting good time intervals, their grouping of their data into energy bins, their use of a smaller aperture, and their lack of pn observations, which supply around 50% of the counts but were often problematic to calibrate 5 years ago. If we also make these choices, we measure a new temperature of $1.27_{-0.11}^{+0.06}$ keV, which agrees with the earlier result.

However, when we reduce our aperture size and bin the spectral data, we find an even lower luminosity; our new bolometric luminosity is $0.79_{-0.05}^{+0.04} \times 10^{43}$ erg s⁻¹. After private communication with S. Bruch, we discovered that the same spectral fitting results were obtained but not published for an aperture of 0.5 Mpc. Using the 4.647 kpc arcsec⁻¹ scale provided in the refereed paper, we extract spectra from a 107.60'' aperture. When letting the abundance vary, we find $T_X = 1.50_{-0.32}^{+0.45}$ keV and $L_{\text{bolo}} = 1.83_{-0.19}^{+0.10} \times 10^{43}$ erg s⁻¹. In addition, we find 252 and 219 net counts for MOS1 and MOS2, respectively. These results are in agreement with the earlier result, which found 231 and 205 counts for the two cameras. We therefore conclude that their reported X-ray aperture radius of 32'' is incorrectly reported, and the actual aperture used was 0.5 Mpc. Using this aperture, we obtain similar results.

RXJ0847.1+3449

[Lumb et al. \(2004\)](#) originally looked at RXJ0847.1+3449 using *XMM-Newton* observation 0107860501. They reported higher values for flux and bolometric luminosity, but a cooler temperature. One source of this difference may

be the larger spectral extraction area they used – it was $120''$, while ours was $\approx 70''$. Therefore we attempted to reproduce their results by using the same aperture and masks, as that work included images of where point sources were excluded.

Bolometric luminosities reported by Lumb et al. (2004) are not for the $120''$ apertures. Rather, they are for apertures scaled to the entire virial radius, as found by using the fitted temperatures and the $T - r_v$ relation of Evrard et al. (1996). In addition, they increased the estimated photon count rate to account for lack of spatial coverage due to chip gaps or masked point sources. We find a comparable luminosity by fitting a MEKAL model to the parameters specified in Table 5 of Lumb et al. (2004). Unlike the reported luminosity, these parameters are for the best fit of the spectrum within $120''$ and are the best measure of what a similar aperture luminosity would be from that work. In order to allow for changes in MEKAL over the past ten years, we let the abundance vary but match the flux reported in the original work.

When fitting to data from the larger aperture, our temperature estimate changes from $4.16^{+0.58}_{-0.39}$ keV to $3.72^{+0.51}_{-0.41}$ keV, which agrees with the reported value of $3.62^{+0.58}_{-0.51}$ keV. Similarly, our flux estimate changes from $5.20^{+0.12}_{-0.14} \times 10^{-14}$ erg s $^{-1}$ cm $^{-2}$ to $6.77^{+0.14}_{-0.12} \times 10^{-14}$ erg s $^{-1}$ cm $^{-2}$, in agreement with the predicted $7.04 \pm 0.3 \times 10^{-14}$ erg s $^{-1}$ cm $^{-2}$. For bolometric luminosity, our value within r_{2500} is $1.31^{+0.04}_{-0.03} \times 10^{44} h_{70}^{-2}$ erg s $^{-1}$, while inside a $120''$ aperture it is $1.70^{+0.06}_{-0.05} \times 10^{44} h_{70}^{-2}$ erg s $^{-1}$. The expected luminosity inside that aperture is $1.75 \times 10^{44} h_{70}^{-2}$ erg s $^{-1}$.

RXJ1354.2–0221

RXJ1354.2–0221 was also originally investigated by Lumb et al. (2004), and, as before, they find a higher flux, higher luminosity, and a lower temperature than we do. As with RXJ0847.1+3449, their technique deviated in aperture size, binning, and definition of luminosity. Additionally, we filtered this data for intervals of flaring differently than they did, which we adjust for in our reanalysis.

We again find a drop in temperature, which changes from $7.60^{+1.92}_{-1.22}$ keV to $3.88^{+0.93}_{-0.59}$ keV when expanding the aperture, in comparison to the originally reported value of $3.66^{+0.6}_{-0.5}$ keV. Likewise, the flux increases from $6.90^{+0.15}_{-0.15} \times 10^{-14}$ erg s $^{-1}$ cm $^{-2}$ to $10.17^{+0.18}_{-0.22} \times 10^{-14}$ erg s $^{-1}$ cm $^{-2}$, which matches the earlier result of $9.8 \pm 0.5 \times 10^{-14}$ erg s $^{-1}$ cm $^{-2}$. Finally, our luminosity rises from $2.11^{+0.10}_{-0.12} \times 10^{44} h_{70}^{-2}$ erg s $^{-1}$ to $2.47^{+0.09}_{-0.06} \times 10^{44} h_{70}^{-2}$ erg s $^{-1}$, which agrees with the predicted expectation of $2.41 \times 10^{44} h_{70}^{-2}$ erg s $^{-1}$. As before, we are able to reproduce the earlier results.

RXJ1117.4+0743

Carrasco et al. (2007) used the same observations analyzed here to look at RXJ1117.4+0743. Their reported temperature ($3.3^{+0.7}_{-0.6}$ keV) is slightly lower than our own ($4.30^{+0.70}_{-0.38}$ keV), but they find larger luminosities from 0.5–2.0 keV (4.19 ± 0.35 to our $1.84^{+0.03}_{-0.03}$, in units of 10^{43} erg s $^{-1}$) and in a bolometric band (11.8 ± 0.9 to our $5.27^{+0.08}_{-0.16}$ in units of 10^{43} erg s $^{-1}$). There are a few differences in our analysis that can bring those results into closer alignment. Along with using a larger aperture – $66''$ to our choice of $47''$ – the previous work binned its data to a minimum of 12 counts per energy bin. Making those adjustments is not enough to match the previous work, however, without also using a different background. In the initial paper, the background was described only as “a larger extraction region near the detector border without any visible sources.” To that end, we used a background centered around $\alpha_{2000} = 11^{\text{h}}17^{\text{m}}40^{\text{s}}$, $\delta_{2000} = +07^{\circ}55^{\text{m}}10^{\text{s}}$ that was $72''$ in size. With this background, we recover similar results to the original reporting: $T_X = 3.13^{+0.30}_{-0.29}$ keV, $F_{[0.5-2.0 \text{ keV}]} = 5.29^{+0.12}_{-0.13} \times 10^{-14}$ erg s $^{-1}$ cm $^{-2}$, $L_{[0.5-2.0 \text{ keV}]} = 3.90^{+0.18}_{-0.14} \times 10^{43}$ erg s $^{-1}$, and $L_{\text{bolo}} = 8.90^{+0.47}_{-0.37} \times 10^{43}$ erg s $^{-1}$. Even without knowing their exact background region, we reproduce the results of Carrasco et al. (2007).

REFERENCES

- Akritas, M. G., & Bershad, M. A. 1996, *ApJ*, **470**, 706
 Allen, S. W., Evrard, A. E., & Mantz, A. B. 2011, *ARA&A*, **49**, 409
 Anders, E., & Grevesse, N. 1989, *Geochim. Cosmochim. Acta*, **53**, 197
 Arnaud, M., Pointecouteau, E., & Pratt, G. W. 2007, *A&A*, **474**, L37
 Bahcall, N. A., & Fan, X. 1998, *ApJ*, **504**, 1
 Belsole, E., Sauvageot, J.-L., Pratt, G. W., & Bourdin, H. 2005, *A&A*, **430**, 385
 Bhattacharya, S., Heitmann, K., White, M., et al. 2011, *ApJ*, **732**, 122
 Bower, R. G. 1997, *MNRAS*, **288**, 355
 Boylan-Kolchin, M., Springel, V., White, S. D. M., Jenkins, A., & Lemson, G. 2009, *MNRAS*, **398**, 1150
 Bruch, S., Donahue, M., Voit, G. M., Sun, M., & Conselice, C. J. 2010, *ApJ*, **724**, 608
 Bryan, G. L., & Norman, M. L. 1998, *ApJ*, **495**, 80
 Carrasco, E. R., Cypriano, E. S., Neto, G. B. L., et al. 2007, *ApJ*, **664**, 777
 Cash, W. 1979, *ApJ*, **228**, 939
 Cavaliere, A., & Fusco-Femiano, R. 1976, *A&A*, **49**, 137
 Eckmiller, H. J., Hudson, D. S., & Reiprich, T. H. 2011, *A&A*, **535**, A105
 Eke, V. R., Cole, S., & Frenk, C. S. 1996, *MNRAS*, **282**, 263
 Ettori, S., & Brighenti, F. 2008, *MNRAS*, **387**, 631
 Evrard, A. E., & Henry, J. P. 1991, *ApJ*, **383**, 95
 Evrard, A. E., Metzler, C. A., & Navarro, J. F. 1996, *ApJ*, **469**, 494
 Fabjan, D., Borgani, S., Tornatore, L., et al. 2010, *MNRAS*, **401**, 1670
 Grossi, M., Dolag, K., Branchini, E., Matarrese, S., & Moscardini, L. 2007, *MNRAS*, **382**, 1261
 Hicks, A. K., Pratt, G. W., Donahue, M., et al. 2013, *MNRAS*, **431**, 2542
 Hoekstra, H., Bartelmann, M., Dahle, H., et al. 2013, *Space Sci. Rev.*, **177**, 75

- Hoekstra, H., Donahue, M., Conselice, C. J., McNamara, B. R., & Voit, G. M. 2011, [ApJ](#), **726**, 48
- Hoekstra, H., Mahdavi, A., Babul, A., & Bildfell, C. 2012, [MNRAS](#), **427**, 1298
- Holder, G., Haiman, Z., & Mohr, J. J. 2001, [ApJ](#), **560**, L111
- Humphrey, P. J., Liu, W., & Buote, D. A. 2009, [ApJ](#), **693**, 822
- Jenkins, A., Frenk, C. S., White, S. D. M., et al. 2001, [MNRAS](#), **321**, 372
- Kaiser, N. 1986, [MNRAS](#), **222**, 323
- . 1991, [ApJ](#), **383**, 104
- Kalberla, P. M. W., Burton, W. B., Hartmann, D., et al. 2005, [A&A](#), **440**, 775
- Kettula, K., Finoguenov, A., Massey, R., et al. 2013, [ApJ](#), **778**, 74
- Klypin, A. A., Trujillo-Gomez, S., & Primack, J. 2011, [ApJ](#), **740**, 102
- LaRoque, S. J., Bonamente, M., Carlstrom, J. E., et al. 2006, [ApJ](#), **652**, 917
- Lumb, D. H., Bartlett, J. G., Romer, A. K., et al. 2004, [A&A](#), **420**, 853
- Mahdavi, A., Hoekstra, H., Babul, A., et al. 2013, [ApJ](#), **767**, 116
- . 2014, [ApJ](#), in press
- Mahdavi, A., Hoekstra, H., Babul, A., & Henry, J. P. 2008, [MNRAS](#), **384**, 1567
- Mantz, A., Allen, S. W., Rapetti, D., & Ebeling, H. 2010, [MNRAS](#), **406**, 1759
- Markevitch, M. 1998, [ApJ](#), **504**, 27
- Matsushita, K., Böhringer, H., Takahashi, I., & Ikebe, Y. 2007, [A&A](#), **462**, 953
- Maughan, B. J. 2007, [ApJ](#), **668**, 772
- Mullis, C. R., McNamara, B. R., Quintana, H., et al. 2003, [ApJ](#), **594**, 154
- Nastasi, A., Böhringer, H., Fassbender, R., et al. 2014, [A&A](#), **564**, A17
- Navarro, J. F., Frenk, C. S., & White, S. D. M. 1997, [ApJ](#), **490**, 493
- Nousek, J. A., & Shue, D. R. 1989, [ApJ](#), **342**, 1207
- Ponman, T. J., Bourner, P. D. J., Ebeling, H., & Böhringer, H. 1996, [MNRAS](#), **283**, 690
- Pratt, G. W., Croston, J. H., Arnaud, M., & Böhringer, H. 2009, [A&A](#), **498**, 361
- Puchwein, E., Sijacki, D., & Springel, V. 2008, [ApJ](#), **687**, L53
- Reichert, A., Böhringer, H., Fassbender, R., & Mühlegger, M. 2011, [A&A](#), **535**, A4
- Rosati, P., Borgani, S., & Norman, C. 2002, [ARA&A](#), **40**, 539
- Rozo, E., Wechsler, R. H., Rykoff, E. S., et al. 2010, [ApJ](#), **708**, 645
- Rykoff, E. S., Evrard, A. E., McKay, T. A., et al. 2008, [MNRAS](#), **387**, L28
- Springel, V., White, S. D. M., Jenkins, A., et al. 2005, [Nature](#), **435**, 629
- Stott, J. P., Hickox, R. C., Edge, A. C., et al. 2012, [MNRAS](#), **422**, 2213
- Strüder, L., Briel, U., Dennerl, K., et al. 2001, [A&A](#), **365**, L18
- Sun, M., Voit, G. M., Donahue, M., et al. 2009, [ApJ](#), **693**, 1142
- Tinker, J., Kravtsov, A. V., Klypin, A., et al. 2008, [ApJ](#), **688**, 709
- Tozzi, P., Gilli, R., Mainieri, V., et al. 2006, [A&A](#), **451**, 457
- Turner, M. J. L., Abbey, A., Arnaud, M., et al. 2001, [A&A](#), **365**, L27
- Vikhlinin, A., McNamara, B. R., Forman, W., et al. 1998, [ApJ](#), **502**, 558
- Vikhlinin, A., Burenin, R. A., Ebeling, H., et al. 2009, [ApJ](#), **692**, 1033
- Voit, G. M. 2005, [Reviews of Modern Physics](#), **77**, 207
- Wachter, K., Leach, R., & Kellogg, E. 1979, [ApJ](#), **230**, 274
- Wall, J. V., & Jenkins, C. R. 2012, [Practical Statistics for Astronomers](#)
- Xue, Y.-J., & Wu, X.-P. 2000, [ApJ](#), **538**, 65